Journal of Materials Chemistry A

PAPER

Cite this: J. Mater. Chem. A, 2016, 4, 6091

Dual function interfacial layer for highly efficient and stable lead halide perovskite solar cells†

Dandan Song,[a] Dong Wei,[a] Peng Cui,[a] Meicheng Li,*[ab] Zhiqiang Duan,[a] Tianyue Wang,[a] Jun Ji,[a] Yaoyao Li,[a] Joseph Michel Mbengue,[a] Yingfeng Li,[a] Yue He,[a] Mwenya Trevor[a] and Nam-Gyu Park[c]

Received 9th February 2016
Accepted 24th March 2016

DOI: 10.1039/c6ta00577b

www.rsc.org/MaterialsA

The trap states and the intrinsic nature of polycrystalline organometallic perovskites cause carrier losses in perovskite solar cells (PSCs) through carrier recombination at the surface and subsurface of the perovskites, leading to lowered conversion efficiency. Herein, to reduce the carrier losses, an intelligent approach concerning surface passivation and interfacial doping of the perovskite is proposed by introducing an F4TCNQ interfacial layer. The trap states at the perovskite surface are efficiently suppressed, leading to a homogenous surface potential of perovskite, which avoids the surface carrier recombination. The Fermi level of the perovskite is shifted to its valence band by 0.2 eV, inducing an energy barrier for electron diffusion and contributing directly to a minimized carrier recombination at the subsurface of the perovskite film. Consequently, the performance of the PSCs is remarkably improved, with the average efficiency increased from 14.3 ± 0.9% to 16.4 ± 1.0% (with a maximum efficiency of 18.1%). Moreover, the PSCs with the dual function interfacial layer show enhanced long-term stability in ambient air without device encapsulation.

Introduction

Lead halide perovskites are a kind of promising active material for solution-processed and low-cost solar cells.[1,2] The power conversion efficiency of perovskite-based solar cells (PSCs) has skyrocketed from 3.8% to more than 20% in the past 5 years.[3–6] Accompanying the rapid progress in device performance, the chemical and physical features of the perovskites are continuously explored to rationalize and further improve their performance in solar cells. The trap states play a great role in the performance of PCSs, and are one of the key factors currently hampering device performance.[7–15] Trap states are present in perovskites due to surface and bulk defects. They induce carrier losses and deteriorate photovoltaic performance of the PSCs.[10–13] Recently, fullerenes (*e.g.* PCBM, C_{60} (ref. 13–16)) have been employed to passivate the trap states at the perovskite surface at the perovskite/electron transport material interface of PSCs,[11–16] leading to remarkable improvement in device performance. On the other hand, the trap states also exist at the perovskite/hole transport material (HTM) interface, with the surface passivation revealed to be positive by a few investigations.[10,11] These limited works are focus on the surface of the perovskite films. However, the region underneath the perovskite surface (*i.e.* the subsurface) also induces carrier losses, correlated with the working principle of the PSCs, and thus needs to be passivated effectively.

In PSCs, the electric field adjacent to the perovskite/HTM interface is inefficient for carrier separation due to the intrinsic or weak self-doping feature of the perovskites,[17–19] together with the organic feature of HTM. Hence, electrons and holes accumulate both at the perovskite surface and at the subsurface of perovskites close to the perovskite/HTM interface (at a depth of tens of nanometres). As a result, carrier losses are prominent both at the surface and subsurface of the perovskites. To enhance the electric field, bulk doping and interfacial doping of the perovskites can be applied. However, increasing the bulk doping concentration of the perovskite leads to deterioration in photovoltaic performance,[20,21] due to the increased carrier recombination. In comparison, the interfacial doping (*i.e.* doping at the perovskite surface) produces only a minor effect on bulk carrier recombination. Consequently, interfacial doping of the perovskite at the perovskite/HTM interface will be effective in enhancing the electric field by largely reducing

[a]State Key Laboratory of Alternate Electrical Power System with Renewable Energy Sources, School of Renewable Energy, North China Electric Power University, Beijing 102206, China. E-mail: mcli@ncepu.edu.cn; Fax: +86 10 6177 2951; Tel: +86 10 6177 2951

[b]Chongqing Materials Research Institute, Chongqing 400707, China

[c]School of Chemical Engineering and Department of Energy Science, Sungkyunkwan University (SKKU), Suwon, 440-746, Korea

† Electronic supplementary information (ESI) available: Simulated electric field and carrier distribution of the standard and modified PSCs, calculated electrical parameters of the standard and modified PSCs, dark *J–V* curves and open circuit voltage decay curves of the standard and modified PSCs, *J–V* curves of the PSCs under different scanning conditions, dark *J–V* curves of the fresh and degraded PSCs, XPS spectra of the standard and modified perovskite films. See DOI: 10.1039/c6ta00577b

carrier losses at the surface and subsurface of the perovskite clinging to this interface.

In the present work, the reduction of carrier losses both at the surface and subsurface of lead halide perovskite ($CH_3NH_3PbI_3$) is achieved through modification with an dual function interfacial layer, 2,3,5,6-tetrafluoro-7,7,8,8-tetracyano-quinodimethane (F4TCNQ), which is typically used to modify the work function of carbonous materials[22] and organic materials.[23] Here, the F4TCNQ interfacial layer has a dual function, namely surface passivation and interfacial doping of the perovskite. In consequence, PSCs based on the F4TCNQ-modified perovskite possess a high conversion efficiency of 18.1% and an enhanced long-term stability in ambient air without device encapsulation.

Results and discussion

An F4TCNQ interfacial layer was prepared by spin-coating its saturated chlorobenzene solution (slightly soluble) on the perovskite surface to achieve an ultrathin film. In this condition, it only modifies the property of the perovskite without having a considerable effect on carrier transport. The morphologies of the pristine and the modified perovskite films were characterized by atomic force microscopy (AFM). The topography of the standard perovskite film (Fig. 1a) exhibits a typical polycrystalline structure with multiple grains. As for the modified perovskite film, the topography in Fig. 1d also presents the typical morphology of the perovskite, indicating the ultrathin thickness of the F4TCNQ layer. To investigate the electronic role of the modification and the trap states at the perovskite surface, a Kelvin probe force microscopy (KPFM) was employed as an efficient tool to characterize the surface states[24] by measuring the local contact potential difference (LCPD) between the sample and the tip. From the potential information shown in Fig. 1b, it is clear that a lower potential appears at the grain boundaries (GBs) and the dark macula. Under irradiation, as presented in Fig. 1c, the overall potential is mildly lowered, whereas the potential of the GBs and the macula are increased. The lowered overall potential correlates with the weak p-type self-doping of the perovskite, in which accumulated holes lead to a lowered surface potential to its valence band (VB). The

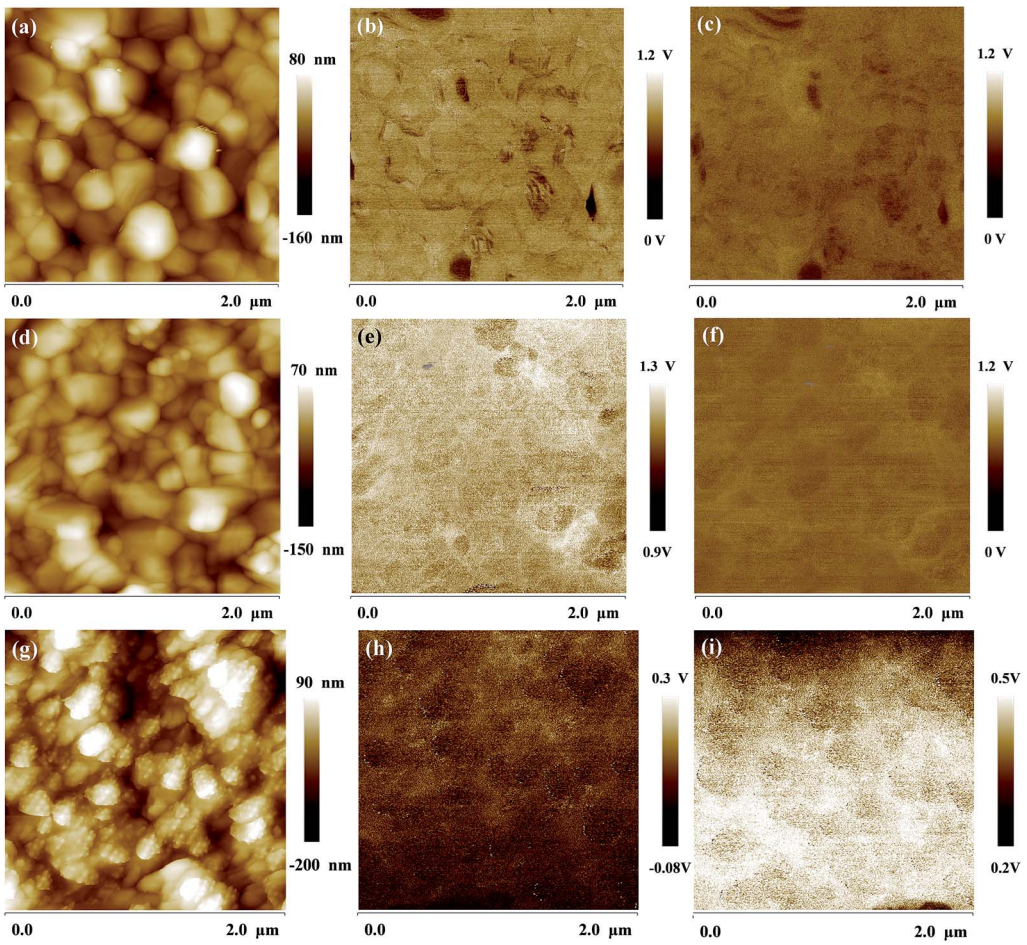

Fig. 1 Topography and surface potential images from a standard perovskite film (a–c), from modified perovskite films (d–f) and from a neat F4TCNQ film (g–i), respectively. (b, e and h) represent the surface potential images measured in the dark, whereas (c, f and i) represent the surface potential images measured under irradiation. It can be seen that neat F4TCNQ shows an amorphous morphology, which is consistent with its organic material feature. The measured dark potential of F4TCNQ is very low due to the small difference between its energy level and the tip potential. Under irradiation, the potential of the F4TCNQ film is increased due to its electron acceptor feature, which accumulates electrons and shifts the potential up to its CB.

increased potential of the GBs and macula represents the shift of the surface potential proximating the conduction band (CB) of the perovskite, which is caused by the capture of the photogenerated electrons through the trap states at the surface and the GBs. Herein, the trap states are identified as acceptor-like traps. The potential image of the modified perovskite film differs from that of the standard one greatly, despite their similar morphologies. As shown in Fig. 1e, the potential at the GBs is slightly higher than that inside the grain, which is opposite to the phenomenon observed from standard perovskite. Under illumination (Fig. 1f), the overall potential also decreases, whereas the spatial potential difference at the modified perovskite surface is much smaller than that at the standard perovskite surface. In addition, the number of the macula is also reduced by modification. F4TCNQ itself yields quite different behaviours in surface potential and photoresponse, as shown in Fig. 1g–i, according to its electron acceptor feature. Therefore, the measured potential differences between standard and modified perovskite films result from the function of F4TCNQ, which reduces the trap states and creates the surface passivation of the perovskite film.

The trap states and their passivation can also be studied by photoluminescence (PL) methods[9,14,15,25] As shown in Fig. 2a, both the band-edge luminescence and the trap-involved luminescence can be observed in the standard perovskite film, whereas only the band-edge luminescence exists in the modified perovskite film. In the perovskites without thermal annealing, the trap-involved luminescence is intense in the standard perovskite film, as shown in Fig. 2b, which is consistent with the existence of a large number of trap states due to the poor crystallinity of the perovskite film without thermal annealing.[21] These trap states can be effectively suppressed by the modification, accompanied by a weaker trap-involved luminescence. It should be pointed out that the passivation of the trap states by modification is not a result of the protection of F4TCNQ to the perovskite film against outer circumstances, because the perovskite film covered by polymethyl methacrylate (PMMA) also shows intense characteristic luminescence of the trap states. The observations from the PL measurements clearly reveal that the surface passivation of perovskite by modification leads to reduced trap states in the perovskite films.

As a strong electron acceptor, the F4TCNQ interfacial layer is able to induce p-type doping of perovskite through the formation of an interfacial dipole layer at the perovskite/F4TCNQ interface. To clarify this role, X-ray photoelectron spectroscopy (XPS) was employed to characterize the surface energy level of the perovskite. XPS energy spectra of the standard and modified perovskite films are shown in Fig. 3a. In the modified perovskite film, there is an additional F 1s bond besides the Pb 4f and I 3d bands, proving the presence of F4TCNQ at the perovskite surface. The VB spectra of the films are presented in Fig. 3b, which show a shift of approximately 0.2 eV of the Fermi level (E_F) after modification, approaching closer to VB, which proves the p-type doping property of F4TCNQ at the perovskite surface. It can be expected that the interfacial doping would also be effective at the subsurface of the perovskite (several nanometres below the surface), therefore XPS presents the material information at a depth of several nanometres.

The interfacial doping of the perovskite creates an energy barrier for the photogenerated electrons, which probably reduce the carrier recombination adjacent to the perovskite/HTM interface. To verify this deduction, the effect of the interfacial doping on carrier recombination in PSCs was simulated using wxAMPS, which is reliable software to simulate thin film solar cells.[26] The modified perovskite was simulated by introducing a 3 nm thick p-type doped region at the perovskite/HTM interface. The electric field adjacent to the perovskite/HTM interface (tens of nanometres away from this interface, as shown in Fig. S1b, ESI†) is enhanced in the PSC with interfacial doping, compared to the standard one. The enhanced

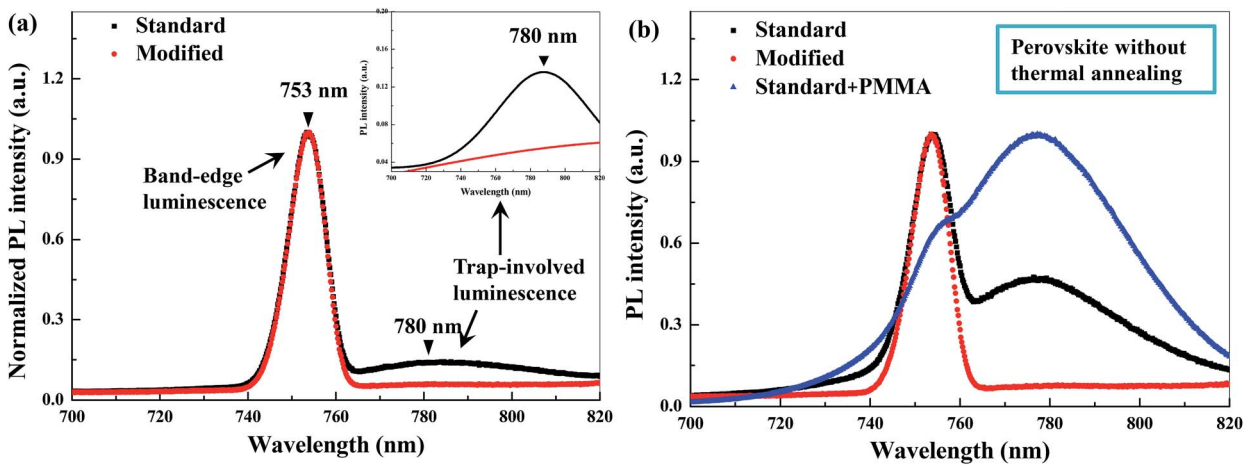

Fig. 2 (a) Schematic of the laser confocal microscopy. (b and c) Spatial PL images from the standard and modified perovskite films. The focus in the 'bulk' is marked by locating the focus at which the film shows the most intense PL intensity. Then, the focus is moved towards the 'surface' by adjusting the *Z* axis of the microscope, stopping at the location that shows a relative clear surface. (d and e) Normalized PL spectra of the standard and modified perovskite films with and without thermal annealing, respectively. Inset of (d) shows the extracted PL spectra in the range of 700 nm to 820 nm by Gaussian fitting.

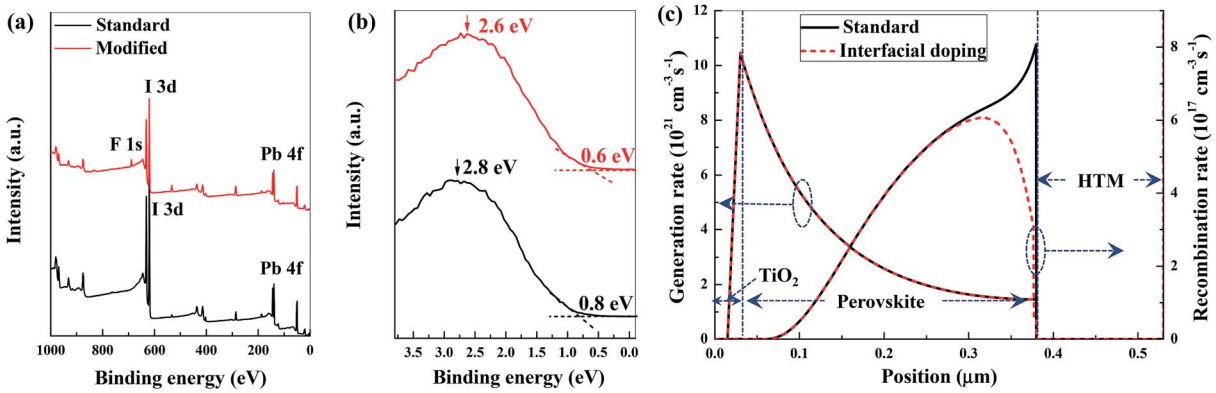

Fig. 3 The interfacial doping of the perovskite with F4TCNQ and its effect on carrier recombination. (a) XPS survey spectra of the perovskite films. (b) XPS valence band spectra of the perovskite films. (c) Simulated generation and recombination rates across the PSCs. It is clear that the recombination rate increases with approximation to the perovskite/HTM interface, due to the lack of electric field at the interface of the intrinsic perovskite/organic HTM. In modified solar cells, the recombination rate is decreased near the perovskite/HTM interface, corresponding to the effect of the enhanced electric field by interfacial doping of the perovskite with F4TCNQ.

electric field promotes electron transport and decreases the concentration of free and trapped electrons adjacent to the perovskite/HTM interface (Fig. S1c and d, ESI†). Hence, the recombination rate is reduced adjacent to the perovskite/HTM interface within the vicinity of tens of nanometres (Fig. 3c) due to the prevented recombination of photogenerated carriers. Therefore, the interfacial doping of the perovskite is valuable in reducing the recombination rate in PSCs, both at the perovskite surface and at the subsurface to a depth of several nanometres adjacent to the perovskite/HTM interface.

The reduced carrier recombination by surface passivation and interfacial doping of the perovskite with the F4TCNQ dual function interfacial layer promotes the harvesting of carriers in PSCs, which will definitely enhance the device performance. Planar PSCs without (standard) and with F4TCNQ (modified) were prepared respectively, as depicted in Fig. 4a. In this architecture, the carrier recombination at the surface and the subsurface clinging to the perovskite/HTM interface were reduced due to the reduced trap states and interfacial doping. The representative photocurrent density–voltage (J–V) curves of the PSCs based on the standard and modified perovskite film are shown in Fig. 4b. The average photovoltaic parameters, including the open circuit voltage (V_{OC}), the short circuit current density (J_{SC}), the fill factor (FF) and the power conversion efficiency (PCE) of the PSCs, are summarized in Table 1. Owing to the introduction of F4TCNQ, all of the photovoltaic parameters are improved, and the PCE is increased from 14.3% (standard PSCs) to 16.4% (modified PSCs), as can be seen from Fig. 4c and Table 1. Hence, the notable improvement in device performance with the F4TCNQ interfacial layer is due to its dual function of surface passivation and interfacial doping, as also evidenced by the J–V curve fitting result (Table S1 and Fig. S2a, ESI†) and by V_{OC} decay curve analysis (Fig. S2b, ESI†).

The trap states in the perovskite/electron transport material interface are reported to be the origin of the photocurrent hysteresis in PCBM-based PSCs, so the reduction of the trap states leads to elimination of the hysteresis.[14,15] However, in TiO_2-based PSCs, *i.e.* the architecture used here, the overall hysteresis is enhanced (Fig. S3, ESI†) in spite of the passivated trap states at the perovskite/HTM interface. The different hysteresis behaviours of PCBM-based PSCs and TiO_2-based PSCs induced by the surface passivation can be explained from the factors determining the hysteresis. In TiO_2-based PSCs, the reduced trap states and the enhanced hole extracting by the F4TCNQ interfacial layer increase the number of holes near the perovskite/HTM interface (Fig. S1d, ESI†). Considering the low

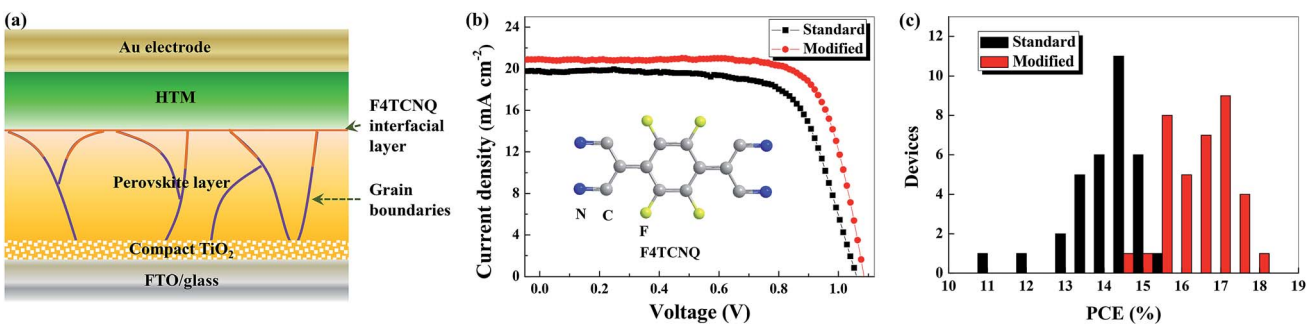

Fig. 4 (a) Schematic of the planar PSCs. (b) J–V curves measured in the reverse scan and the molecular structure of F4TCNQ. (c) Efficiency distribution of multiple PSCs (36 identical PSCs for each type of solar cell).

Table 1 Photovoltaic parameters of the PSCs without (standard) and with F4TCNQ modification (modified). The PSCs were degraded in ambient air without encapsulation for 40 days (960 h). The standard deviations of the photovoltaic parameters were calculated from multiple PSCs

PSCs		V_{OC} (V)	J_{SC} (mA cm^{-2})	FF (%)	PCE (%)	Highest PCE (%)
Standard	Fresh	1.04 ± 0.03	19.4 ± 0.9	69.9 ± 2.8	14.3 ± 0.9	15.3
	Degraded	1.00 ± 0.02	13.5 ± 1.5	43.3 ± 6.6	5.8 ± 1.0	7.1
Modified	Fresh	1.06 ± 0.01	20.3 ± 0.8	75.4 ± 2.7	16.4 ± 1.0	18.1
	Degraded	1.04 ± 0.01	15.2 ± 1.1	64.5 ± 4.6	10.2 ± 1.4	13.5

hole mobility of the organic HTM, holes accumulate near the perovskite/HTM interface, which causes additional hysteresis. In this context, the hysteresis in modified PSCs is still obvious. Based on these analyses, it can be speculated that TiO_2-based PSCs employing HTM with high hole mobility will simultaneously achieve elimination of the photocurrent hysteresis and a high performance through modification of the perovskite with F4TCNQ.

Furthermore, the long-term stability of the PSCs is significantly improved by the dual function interfacial layer. As shown in Fig. 5a and as listed in Table 1, standard PSCs without encapsulation show serious degradation in photovoltaic performance after exposition in ambient air for 40 days. In comparison, modified PSCs without encapsulation show much better stability, maintaining more than 60% of the initial PCE and enabling a lifetime (degradation to 50%) of over 1000 h. The improved device stability can also be ascribed to the surface passivation of the perovskite by the F4TCNQ interfacial layer. It was found that the degradation of the PSCs is in accordance with the increased density of the trap states (Fig. S4, ESI†). The trap states enhance the carrier recombination, causing a lower J_{SC} and FF of the PSCs. Hence, J_{SC} and FF degrade more dramatically (Fig. 5a), leading to the low PCE of the degraded PSCs. In comparison, the morphology evolution of the perovskite films and decomposition of the perovskite are not observed (Fig. 5b–d), thus excluding their effects on the long-term stability of the PSCs. Herein, the reduction of the trap states in the modified PSCs is the main origin of their superior long-term stability compared to the standard PSCs. Deep insights into the correlation between the trap states and the long-term stability of the PSCs remain to be explored in future investigations.

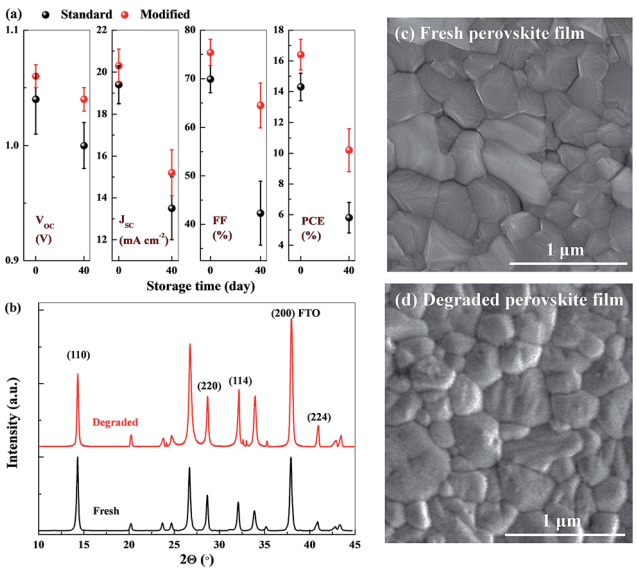

Fig. 5 (a) Photovoltaic parameters of the standard and modified PSCs measured immediately after fabrication and after storage for 40 days in the dark in ambient air (humidity 50–70%, 22 °C). (b) X-ray diffraction (XRD) patterns of the fresh and degraded standard perovskite films. (c and d) Scanning electron microscope (SEM) images of the fresh (c) and degraded (d) standard perovskite films. The fresh perovskite films were obtained by depositing perovskite on an FTO/glass substrate, while the degraded perovskite film was obtained by removing the Au electrode and HTM from the standard perovskite solar cells. Removal of the Au electrode was carried out by the tape-peeling off method,[27] whereas removal of HTM was achieved by washing the film with chlorobenzene three times.[28] The degradation lasted for more than 40 days.

The dual function F4TCNQ interfacial layer with surface passivation and interface doping of the perovskite enables an excellent photovoltaic performance of the related PSCs. The underlying relationships between these factors are depicted in Fig. 6. The traps states formed by iodine ions[10,15] cause recombination of the carriers at the surface and grain boundaries, as illustrated in Fig. 6a. The strong electron acceptor characteristic of F4TCNQ enables it to form a supramolecular interaction with halide ions (iodine ions in the perovskite) through halogen bonding. Accordingly, the trap states at the perovskite surface and the grain boundaries can be passivated by F4TCNQ. Furthermore, the LUMO level of F4TCNQ (5.23 eV) lies below the Fermi level of the perovskite (around 4.6 eV, according to the 0.8 eV difference between its E_F and VB). Hence, electrons will diffuse from perovskite to F4TCNQ, forming an interfacial dipole layer at the perovskite/F4TCNQ interface (as shown in Fig. 6b), with the positive charges lying in the perovskite side, leading to an enhanced electric field adjacent to the perovskite/HTM interface. The electron diffusion shifts the Fermi level towards the VB of the perovskite, *i.e.* an up-bending of the VB at the interface (Fig. 6c), which is typically considered as 'p-type doping'. From the energy level diagram shown in Fig. 6c, it is clear that the p-type doping of the perovskite by F4TCNQ creates an energy barrier to electron diffusion, which effectively reduces recombination of the photogenerated carriers near the perovskite/HTM interface. Hence, carrier recombination at the surface and subsurface of the perovskite are suppressed, resulting in a high J_{SC}, V_{OC} and resultant FF and PCE in the modified PSCs. The increase in V_{OC} (20 mV) after F4TCNQ modification is not as much as the E_F shift (0.2 eV) of the perovskite by interfacial doping, which is reasonable

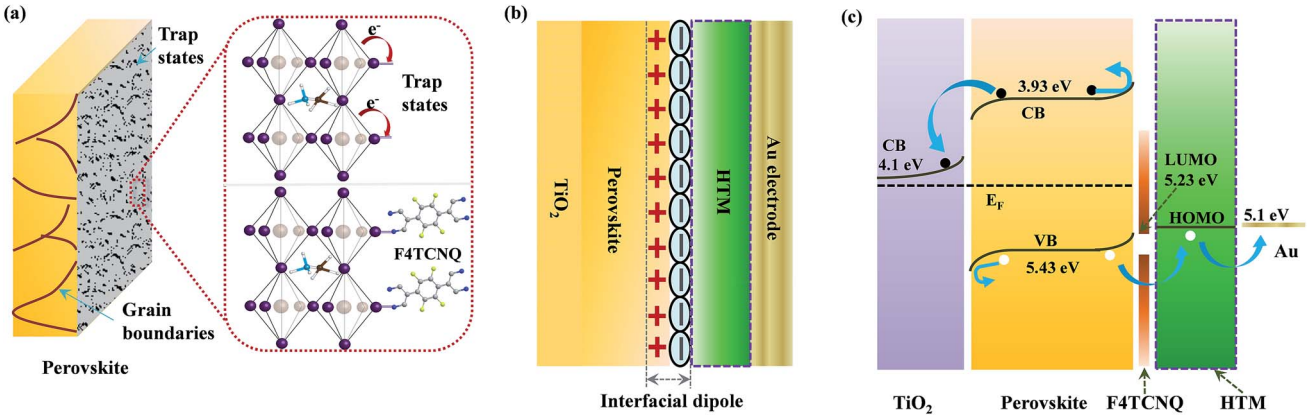

Fig. 6 Schematic for reduced recombination at the surface and subsurface by surface passivation and interfacial doping with the F4TCNQ dual function interfacial layer. (a) The role of the trap states in trapping electrons and their passivation with F4TCNQ. In $CH_3NH_3PbI_3$, the trap states are probably caused by surface iodine ions. In addition, XPS also shows that the atom ratio of Pb to I (1 : 4), as calculated from the integration of the Pb 4f and I 4d spectra (Fig. S5 ESI†), is lower than their stoichiometric ratio of 1 : 3, revealing the existence of excess iodine elements in the perovskite, at least near its surface. (b) Interfacial doping of the perovskite by the interface dipole induced by the electron diffusion from the perovskite to the lowest unoccupied molecular orbital (LUMO) of F4TCNQ. The dipole layer enhances the electric field at the perovskite/HTM interface, which can then block the electron diffusion but favour the hole diffusion from the inner perovskite to the surface. (c) Energy level diagram of the PSCs with the modified perovskite.

considering the working principle of the PSCs. As V_{OC} is determined by the potential difference between the quasi-E_F of TiO_2 and the highest occupied molecular orbital (HOMO) level of HTM under irradiation, thus the variation in the E_F of the perovskite is not able to directly vary the V_{OC}. The increase in V_{OC} by F4TCNQ modification is instead due to the effect of the reduced bulk recombination by interfacial doping.

Conclusion

In conclusion, an F4TCNQ dual function interfacial layer was first introduced to modify the surface and subsurface properties of the perovskite in PSCs, which induced surface passivation and interfacial doping of the intrinsic perovskite. The carrier recombination at both the surface and subsurface of the perovskite was efficiently reduced, leading to improved photovoltaic performance of the PSCs. Moreover, the long-term stability of the PSCs was also dramatically improved, with the degradation amplitude decreasing from 60% to less than 40%. These findings highlight the crucial role of the interfacial layer at the perovskite/HTM interface for achieving highly efficient and stable perovskite solar cells.

Experimental

Fabrication of $CH_3NH_3PbI_3$ films and PSCs

$CH_3NH_3PbI_3$ films were fabricated using a sequential deposition process. PbI_2 was first dissolved in dimethylsulfoxide (DMSO) (1 mol mL^{-1}) and then kept at 70 °C for one day to achieve intensive dissolution. Then, PbI_2 solution was filtered with a 0.45 μm filter and loaded onto a compact TiO_2 layer (for solar cell fabrication), FTO/glass substrates (for XPS and KPFM characterization) or glass substrates (for PL characterization) by spin-coating at a speed of 3000 rpm for 30 s, repeated three times. Then, the as-fabricated yellow PbI_2 films were dipped into a solution of CH_3NH_3I (40 mg mL^{-1}) in ultra-dry isopropanol for 10 min to form dark red, homogenous $CH_3NH_3PbI_3$ films. Afterwards, the $CH_3NH_3PbI_3$ films were post-annealed at 150 °C for 30 min. All of the procedures were carried out in the glove box filled with high purity N_2.

The PSCs employ the planar architecture of FTO/compact TiO_2/perovskite (~300 nm)/HTM/Au electrode. The active device area was 5 mm^2. The compact TiO_2 layer (approximate 25 nm) was fabricated on FTO/glass substrates by $TiCl_4$ treatment.[29] Modification of the perovskite was carried out by spin-coating F4TCNQ chlorobenzene solution at 6000 rpm, followed by thermal annealing at 60 °C for 5 min. The thermal annealing stabilized F4TCNQ on the perovskite surface, preventing it being washed away in the process of depositing the HTM layer. The HTM layer was obtained by spin-coating (5000 rpm) the 2,2′,7,7′-tetrakis[*N*,*N*-di(4-methoxyphenyl)amino]-9,9′-spirobifluorene (spiro-MeOTAD) solution (dissolved in chlorobenzene with a concentration of 80 mg mL^{-1}) with the standard additives *tert*-butylpyridine and lithium bis(trifluoro methane sulfonyl)imide in the glove box, followed by degradation in clean air for 2 h. Afterwards, the Au electrode was prepared by magnetron sputtering.

Characterization

Kelvin probe force microscopy (KPFM) measurements were carried out using the Agilent SPM 5500 instrument with the sample chamber filled with high purity N_2. KPFM was measured in the tapping mode. No voltage was applied between the sample and the tip. Irradiation of the samples was conducted using a Xe lamp, with the light output coupled by a fibre inserted in the sample chamber. Current density–voltage curves of the PSCs were measured using a source meter (Keithley 2400) at a scan rate of 160 mV s^{-1} without a mask under AM 1.5G irradiation with a power density of 100 mW cm^{-2} from a solar simulator (XES-301S+EL-100).

Device simulation

Device simulation was carried out using wxAMPS software, based on the planar architecture of FTO/compact TiO_2 (30 nm)/perovskite (350 nm)/HTM (150 nm)/Au electrode. The doping concentrations, mobility and other properties of the materials were referred to the literature[20,30–33] The perovskite was set to be intrinsic without doping, whereas the interfacial doping of the perovskite was modulated by using a 3 nm thick p-type doped perovskite (with a doping concentration of 10^{18} cm^{-3}).

Acknowledgements

This study was supported partially by the National High-tech R&D Program of China (863 Program, No. 2015AA034601), the National Natural Science Foundation of China (Grant no. 91333122, 61204064, 51202067, 51372082, 51402106 and 11504107), Ph.D. Programs Foundation of Ministry of Education of China (Grant no. 20120036120006, 20130036110012), Par-Eu Scholars Program, and the Fundamental Research Funds for the Central Universities.

References

1 M. M. Lee, J. Teuscher, M. Tsutomu, T. N. Murakami and H. J. Snaith, *Science*, 2012, **338**, 643–647.
2 B. Julian, P. Norman, M. Soo-Jin, H. B. Robin, G. Peng, M. K. Nazeeruddin and G. T. Michael, *Nature*, 2013, **499**, 316–319.
3 H. Zhou, Q. Chen, G. Li, S. Luo, T. B. Song, H. S. Duan, Z. Hong, J. You, Y. Liu and Y. Yang, *Science*, 2014, **345**, 542–546.
4 J. H. Im, C. R. Lee, J. W. Lee, S. W. Park and N. G. Park, *Nanoscale*, 2011, **3**, 4088–4093.
5 H. S. Kim, C. R. Lee, J. H. Im, K. B. Lee, T. Moehl, A. Marchioro, S. J. Moon, R. Humphry-Baker, J. H. Yum, J. E. Moser, M. Grätzel and N. G. Park, *Sci. Rep.*, 2012, **2**, 591.
6 K. Akihiro, T. Kenjiro, S. Yasuo and M. Tsutomu, *J. Am. Chem. Soc.*, 2009, **131**, 6050–6051.
7 P. Cui, P. Fu, D. Wei, M. Li, D. Song, X. Yue, Y. Li, Z. Zhang, Y. Li and J. M. Mbengue, *RSC Adv.*, 2015, **5**, 341–344.
8 G. J. A. H. Wetzelaer, S. Max, S. Araceli Miquel, M. Cristina, Á. Jorge and H. J. Bolink, *Adv. Mater.*, 2015, **27**, 344–347.
9 D. W. de Quilettes, S. M. Vorpahl, S. D. Stranks, H. Nagaoka, G. E. Eperon, M. E. Ziffer, H. J. Snaith and D. S. Ginger, *Science*, 2015, **348**, 683–686.
10 A. Abate, M. Saliba, D. J. Hollman, S. D. Stranks, K. Wojciechowski, R. Avolio, G. Grancini, A. Petrozza and H. J. Snaith, *Nano Lett.*, 2014, **14**, 3247–3254.
11 N. K. Noel, A. Abate, S. D. Stranks, E. S. Parrott, V. M. Burlakov, A. Goriely and H. J. Snaith, *ACS Nano*, 2014, **8**, 9815–9821.
12 H. Azimi, T. Ameri, H. Zhang, Y. Hou, C. O. R. Quiroz, J. Min, M. Hu, Z. G. Zhang, T. Przybilla and G. J. Matt, *Adv. Energy Mater.*, 2015, **5**, 3247–3254.
13 Q. Wang, Y. Shao, Q. Dong, Z. Xiao, Y. Yuan and J. Huang, *Energy Environ. Sci.*, 2014, **7**, 2359–2365.
14 Y. Shao, Z. Xiao, C. Bi, Y. Yuan and J. Huang, *Nat. Commun.*, 2014, **5**, 5784.
15 J. Xu, A. Buin, A. H. Ip, W. Li, O. Voznyy, R. Comin, M. Yuan, S. Jeon, Z. Ning and J. J. McDowell, *Nat. Commun.*, 2015, **6**, 1401692.
16 P. W. Liang, C. C. Chueh, S. T. Williams and A. K. Y. Jen, *Adv. Energy Mater.*, 2015, **5**, 201402321.
17 C. C. Stoumpos, C. D. Malliakas and M. G. Kanatzidis, *Inorg. Chem.*, 2013, **52**, 9019–9038.
18 C. Bi, Y. Shao, Y. Yuan, Z. Xiao, C. Wang, Y. Gao and J. Huang, *J. Mater. Chem. A*, 2014, **2**, 18508–18514.
19 W. J. Yin, T. Shi and Y. Yan, *Appl. Phys. Lett.*, 2014, **104**, 063903–063904.
20 Q. Wang, Y. Shao, H. Xie, L. Lyu, X. Liu, Y. Gao and J. Huang, *Appl. Phys. Lett.*, 2014, **105**, 163508.
21 D. Song, P. Cui, T. Wang, D. Wei, M. Li, F. Cao, X. Yue, P. Fu, Y. Li, Y. He, B. Jiang and M. Trevor, *J. Phys. Chem. C*, 2015, **119**, 22812–22819.
22 D. Qi, C. Wei, X. Gao, W. Li, C. Shi, K. P. Loh and A. T. S. Wee, *J. Am. Chem. Soc.*, 2007, **129**, 8084.
23 K. Norbert, *ChemPhysChem*, 2007, **8**, 1438–1455.
24 W. Melitz, J. Shen, A. C. Kummel and S. Lee, *Surf. Sci. Rep.*, 2011, **66**, 1–27.
25 X. Wu, M. T. Trinh, D. Niesner, H. Zhu, Z. Norman, J. S. Owen, O. Yaffe, B. J. Kudisch and X. Y. Zhu, *J. Am. Chem. Soc.*, 2015, **137**, 2089–2096.
26 Y. Liu, Y. Sun and A. Rockett, *Sol. Energy Mater. Sol. Cells*, 2012, **98**, 124–128.
27 Q. Wang, G. Williams, T. Tsui and H. Aziz, *J. Appl. Phys.*, 2012, **112**, 064502–064507.
28 D. Wei, T. Wang, J. Ji, M. Li, P. Cui, Y. Li, G. Li, J. M. Mbengue and D. Song, *J. Mater. Chem. A*, 2016, **4**, 1991–1998.
29 A. Yella, L. P. Heiniger, P. Gao, M. K. Nazeeruddin and M. Grätzel, *Nano Lett.*, 2014, **14**, 2591–2596.
30 T. Leijtens, J. Lim, J. Teuscher, T. Park and H. J. Snaith, *Adv. Mater.*, 2013, **25**, 3227–3233.
31 F. Liu, J. Zhu, J. Wei, Y. Li, M. Lv, S. Yang, B. Zhang, J. Yao and S. Dai, *Appl. Phys. Lett.*, 2014, **104**, 253508.
32 S. D. Wolf, J. Holovsky, S. J. Moon, P. Löper, B. Niesen, M. Ledinsky, F. J. Haug, J. H. Yum and C. Ballif, *J. Phys. Chem. Lett.*, 2014, **5**, 1035–1039.
33 C. Wehrenfennig, G. E. Eperon, M. B. Johnston, H. J. Snaith and L. M. Herz, *Adv. Mater.*, 2014, **26**, 1584–1589.